Simulation of multicomponent fluids in complex three-dimensional geometries by the lattice Boltzmann method

Nicos S. Martys[1] and Hudong Chen[2]
[1]National Institute of Standards and Technology, Building Materials Division, 226/B348, Gaithersburg, Maryland 20899
[2]Exa Corporation, 125 Cambridge Park Street, Cambridge, Massachusetts 02140
(Received 11 July 1995)

We describe an implementation of the recently proposed lattice Boltzmann based model of Shan and Chen [Phys. Rev. E **47**, 1815 (1993); **49**, 2941 (1994)] to simulate multicomponent flow in complex three-dimensional geometries such as porous media. The above method allows for the direct incorporation of fluid-fluid and fluid-solid interactions as well as an applied external force. As a test of this method, we obtained Poiseuille flow for the case of a single fluid driven by a constant body force and obtained results consistent with Laplace's law for the case of two immiscible fluids. The displacement of one fluid by another in a porous medium was then modeled. The relative permeability for different wetting fluid saturations of a microtomography-generated image of sandstone was calculated and compared favorably with experiment. In addition, we show that a first-order phase transition, in three dimensions, may be obtained by this lattice Boltzman method, demonstrating the potential for modeling phase transitions and multiphase flow in porous media.

PACS number(s): 47.55.Mh

I. INTRODUCTION

Fluid flow in porous media plays an important role in a wide variety of technological and environmental [1] processes such as chromatography, oil recovery, the degradation of building materials, and the spread of hazardous wastes in soils. The displacement of one fluid by another also exhibits a rich variety of pattern formation including a fractal or self-affine growth morphology [2]. Such diverse behavior is a consequence of growth mechanisms that depend on the fluid properties (such as viscosity or surface tension), the structure of the porous medium, and the external driving force that displaces the fluids. The complexity of multicomponent fluid flow in random porous media makes it theoretical and experimental study a great challenge.

Recently there has been significant progress in the development of computational fluid dynamics methods based on cellular automata [3,4] ideas called lattice gas automata (LGA) and lattice Boltzmann (LB). Early versions of LGA and LB methods were plagued by systematic problems such as velocity-dependent pressures and the lack of Galilean invariance. However, key progress has been made in both LGA and LB methods, such that the above well-known problems are essentially resolved [5–9]. Also, for many applications, LB algorithms have been simplified through use of the single relaxation time scheme of Bhatnager, Gross, and Krook [5,7,8,10].

LGA and LB methods have shown great potential for the modeling of multicomponent fluid flow in porous media [11]. LGA and LB methods can naturally incorporate interactions between different fluids and between fluids and solids. Furthermore, LGA and LB methods are ideally suited for computation on parallel computers since most algorithms only depend on nearest-neighbor information. Over the past few years, there have been several efforts to extend LGA and LB methods for the study of immiscible fluids and flow in porous media. The first LGA model of immiscible fluids was formulated by Rothman and Keller [12]. In addition to the usual collision dynamics of LGA, they model immiscible fluids by introducing a mechanism that, according to information at neighboring lattice cells, alters the particle distributions at each lattice cell enabling the pressure tensor to become anisotropic near the fluid-fluid interface. This mechanism redirects the momentum of particles of each given fluid component according to the gradient of a "color" field defined by the spatial distributions of the components. As a result, an effective surface tension force is produced that separates different fluids. This approach was first extended to LB methods by Gunstensen *et al.* [13,14] and further developed by others [15,16], and has been applied to the study of multicomponent flow in porous media [17].

More recently, an alternative LB approach to modeling immiscible fluids has been developed by Shan and Chen [18,19] (SC). Their approach involves the introduction of an external force at each cell as a function of neighboring cell properties. This force is used to modify the momentum values in the equilibrium distributions at the cell. A distinct feature of this formalism is that, although at each local cell there is a gain or loss of momentum, the global momentum conservation of the system is still exactly satisfied when boundary effects are excluded. Furthermore, all forces on a fluid can be easily related to an interaction potential. In contrast to earlier LB methods, this approach also has the capability of modeling thermodynamic first-order phase transitions [20] in single-component fluid. Earlier results of SC were presented for

1063-651X/96/53(1)/743(8)/$06.00

the cases of two-dimensional (2D) hexagonal and four-dimensional face-centered hypercubic (FCHC) lattices. In this paper we adopt this latter formalism to study the flow of a multicomponent fluid subject to gravitational and surface tension forces in complex three-dimensional geometries such as porous media.

This paper is organized in the following way. In Sec. II, a brief review of the LB method and the concept for dealing with fluid interactions is then given in Sec. III. The projection of the 4D FCHC LB model to the three-dimensional space, which is an extension of the 3DQ19 LB model of Qian, d'Humières, and Lallemand [7] is then described in Sec. IV. To make a connection with the original 4D model, we compare, in Sec. IV, the simulation result of a first-order phase transition in the 3D model of a single-component fluid at the critical point with the theory. We next show, in Sec. V, how to introduce a constant force on a fluid such as gravity. As a test case, we simulate fluid flow between parallel plates driven by a constant gravitational field and obtain Poiseuille [21] flow. In Sec. VI we describe the modeling of surface tension forces between two fluids. Section VII describes a simple ansatz to incorporate forces between a fluid and a solid wall. We show that arbitrary static contact angles may be obtained by varying the surface tension force. This is followed by Sec. VIII in which we combine the above techniques and present results of simulations of multicomponent fluid flow in porous media. A relative permeability curve for wetting and nonwetting fluids was calculated using a porous medium based on a microtomography image of sandstone. Relative permeability results are compared with recent experiments. Section IX contains conclusions and comments.

II. LATTICE BOLTZMANN METHOD

In this section we present a brief description of the LB method. The basic approach of the LB method is to construct a lattice on which one solves for the evolution of a particle distribution function that obeys a lattice Boltzmann equation (in contrast to the LB method, the LGA method describes the evolution of individual particles on a lattice). The distribution function $n_a^\sigma(\mathbf{x},t)$, where the superscript σ labels the fluid component and the subscript indicates the velocity direction, is the amount of particles at node $\mathbf{x}$, time t, and velocity $\mathbf{e}_a$ where $a=1,\ldots,b$. The magnitude of $\mathbf{e}_a$ is equal to c, the lattice constant divided by the time step. Macroscopic quantities such as density $\rho^\sigma(\mathbf{x},t)$ and fluid velocity $\mathbf{u}^\sigma$ of each fluid component σ are then easily obtained from these distributions as simple moment sums

$$\rho^\sigma(\mathbf{x},t)=\sum_a m^\sigma n_a^\sigma(\mathbf{x},t) \tag{1}$$

and

$$\mathbf{u}^\sigma(\mathbf{x},t)=\frac{\sum_\sigma m^\sigma \sum_a n_a^\sigma(\mathbf{x},t)\mathbf{e}_a}{\rho^\sigma(\mathbf{x},t)} , \tag{2}$$

where m^σ is the molecular mass of the σth component. The evolution of the particle distribution function satisfies the lattice Boltzmann equation

$$n_a^\sigma(\mathbf{x}+\mathbf{e}_a,t+1)-n_a^\sigma(\mathbf{x},t)=\Omega_a^\sigma(\mathbf{x},t) , \tag{3}$$

where Ω_a^σ is the collision operator representing the rate of change of the particle distribution due to collisions. The collision operator is greatly simplified by use of the single time relaxation approximation [5,7,10]

$$\Omega_a^\sigma(\mathbf{x},t)=-\frac{1}{\tau_\sigma}[n_a^\sigma(\mathbf{x},t)-n_a^{\sigma(\mathrm{eq})}(\mathbf{x},t)] , \tag{4}$$

where $n_a^{\sigma(\mathrm{eq})}(\mathbf{x},t)$ is the equilibrium distribution at $\mathbf{x},t$ and τ_σ is the relaxation time that controls the rate of approach to equilibrium. The equilibrium distribution can be represented in the following form for particles of each type [18]:

$$n_0^{\sigma(\mathrm{eq})}(\mathbf{x})=n^\sigma(\mathbf{x})\left[d_0-\frac{1}{c^2}\mathbf{u}^2\right] , \tag{5}$$

$$n_a^{\sigma(\mathrm{eq})}(\mathbf{x})=n^\sigma(\mathbf{x})\left[\frac{1-d_0}{b}+\frac{D}{c^2 b}\mathbf{e}_a\cdot\mathbf{u}+\frac{D(D+2)}{2c^4 b}\mathbf{e}_a\mathbf{e}_a:\mathbf{u}\mathbf{u}-\frac{D}{2bc^2}\mathbf{u}^2\right] , \tag{6}$$

where

$$\mathbf{u}=\frac{\sum_\sigma^S m^\sigma \sum_a n_a^\sigma \mathbf{e}_a/\tau_\sigma}{\sum_\sigma^S m^\sigma n^\sigma(\mathbf{x})/\tau_\sigma} \tag{7}$$

and d_0 is the fraction of particles with zero speed in equilibrium. It has been shown that the above formalism leads to a velocity field that is a solution of the Navier-Stokes [9] equation with the kinematic viscosity [22] ν,

$$\nu=c^2\frac{\sum_\sigma^S c_\sigma\tau_\sigma-\frac{1}{2}}{D+2} , \tag{8}$$

where c_σ is the concentration of each component. The above form of LB equations is typically used for single speed lattices such as the two-dimensional hexagonal ($b=6$) and the four-dimensional FCHC ($b=24$). We will later consider the projection from four dimensions to three dimensions.

III. INTERACTION POTENTIAL

To model surface tension forces in multicomponent fluids or fluids that are characterized by a nonideal gas equation of state, the interaction potential $V(\mathbf{x},\mathbf{x}')$ can be incorporated [18]:

$$V(\mathbf{x},\mathbf{x}')=G_{\sigma\sigma'}\psi^\sigma(\mathbf{x})\psi^{\sigma'}(\mathbf{x}') , \tag{9}$$

where $\psi^\sigma(\mathbf{x})=F^\sigma(n(\mathbf{x}))$ is a function of $n(\mathbf{x})$ and $G_{\sigma\sigma}(\mathbf{x},\mathbf{x})$ is the interaction strength. Assuming that $G_{\sigma\sigma'}$ involves only nearest-neighbor interactions for simplicity, the rate of change of momentum at each site is

$$\frac{dp^\sigma}{dt}(\mathbf{x})=-\psi^\sigma(\mathbf{x})\sum_{\sigma'}^S G_{\sigma\sigma'}\sum_{a=0}^b \psi^{\sigma'}(\mathbf{x}+\mathbf{e}_a)\mathbf{e}_a . \tag{10}$$

The new momentum at each site for each component then becomes

$$n^{\sigma}(\mathbf{x})\mathbf{u}'(\mathbf{x})=n^{\sigma}\mathbf{u}(\mathbf{x})+\tau_{\sigma}\frac{dp^{\sigma}}{dt}(\mathbf{x}) , \tag{11}$$

where $\mathbf{u}'$ is the new velocity used in Eqs. (5) and (6).

IV. PROJECTION FROM FOUR TO THREE DIMENSIONS

To carry out calculations in three dimensions we projected the above formalism from the 4D FCHC lattice to the D3Q19 model described by Qian, d'Humières, and Lallemand where D is the dimension and Q is the number of velocity directions (or states) [7]. The projection involves doubling the population of states that have a single nonvanishing velocity component. For instance, a component corresponding to the velocity vector (1,0,0) in the D3Q19 model is a combination of the (1,0,0,1) and (1,0,0,−1) components from the 4D FCHC lattice (see the Appendix). By combining such components one arrives at the following equilibrium equation from Eqs. (5) and (6):

$$n_0^{\sigma(\mathrm{eq})}(\mathbf{x})=\tfrac{1}{3}n^{\sigma}(\mathbf{x})[1-\tfrac{3}{2}\mathbf{u}^2] , \tag{12}$$

$$n_a^{\sigma(\mathrm{eq})}(\mathbf{x})=t_i n^{\sigma}(\mathbf{x})[1+3\mathbf{e}_a\cdot\mathbf{u}+\tfrac{3}{2}(3\mathbf{e}_a\mathbf{e}_a:\mathbf{u}\mathbf{u}-\mathbf{u}^2)] , \tag{13}$$

where we have taken $d_0=\frac{1}{3}$, $b=24$, $D=4$, $c^2=2$, and here $t_1=\frac{1}{18}$ and $t_2=\frac{1}{36}$. Equations (12) and (13) were originally obtained by Qian, d'Humières, and Lallemand [7].

While the form of the interaction potential and force term [Eqs. (9) and (10)] is the same for both D3Q19 and the FCHC lattice, care must be taken to carry over results from four to three dimensions. Consider the case of a nearest-neighbor interaction in four dimensions. Assuming there is no variation of density along the fourth dimension, the force equation can be written

$$\frac{dp^{\sigma}}{dt}(\mathbf{x})=-\psi^{\sigma}(\mathbf{x})\sum_{\sigma'}^{S}G_{\sigma\sigma'}\left[\sum_{a_0}\psi^{\sigma'}(\mathbf{x}+\mathbf{e}_a)\mathbf{e}_a+\sum_{a_+}\psi^{\sigma'}(\mathbf{x}+\mathbf{e}_a)\mathbf{e}_a+\sum_{a_-}\psi^{\sigma'}(\mathbf{x}+\mathbf{e}_a)\mathbf{e}_a\right] , \tag{14}$$

where a_0 includes states that have zero fourth components and a_+, a_- correspond to states that have positive and negative fourth components, respectively. Note that states with zero fourth components correspond to the diagonal states in D3Q19. Therefore we can write

$$\frac{dp^{\sigma}}{dt}(\mathbf{x})=-\psi^{\sigma}(\mathbf{x})\sum_{\sigma'}^{S}G_{\sigma\sigma'}\left[\sum_{\mathrm{diag}}\psi^{\sigma'}(\mathbf{x}+\mathbf{e}_a)\mathbf{e}_a+2\sum_{\mathrm{nondiag}}\psi^{\sigma'}(\mathbf{x}+\mathbf{e}_a)\mathbf{e}_a\right] . \tag{15}$$

As can be seen, the nearest-neighbor interaction in four dimensions corresponds to a potential that couples nearest and next nearest neighbors in the D3Q19 lattice model. In this case,

$$\frac{dp^{\sigma}}{dt}(\mathbf{x})=-\psi^{\sigma}(\mathbf{x})\sum_{\sigma'}^{S}\sum_{a}G_{\sigma\sigma'}^{a}\psi^{\sigma'}(\mathbf{x}+\mathbf{e}_a)\mathbf{e}_a , \tag{16}$$

$$G_{\sigma\sigma'}^{a}=\begin{cases}2G & \text{for } |\mathbf{e}^a|=1\\ G & \text{for } |\mathbf{e}^a|=\sqrt{2}\\ 0 & \text{otherwise ,}\end{cases}$$

where G is a constant. To test this approach we tried modeling a first-order phase transition as described by SC [18]. Here we take $\psi(\mathbf{x})=1-\exp[-n(\mathbf{x})]$. The predicted value of the critical coupling [18], where the phase transition takes place, is $G_c=-4(1-d_0)/b=\frac{1}{9}$ ($d_0=\frac{1}{3}, b=24$). Figure 1 shows the difference between the maximum and the minimum density in a single fluid as a function of G. Clearly there is a transition to two phases at the predicted value of G_c.

V. EXTERNAL FORCE: GRAVITY

It is straightforward to introduce the action of a constant body force, such as gravity, on the fluid. The force term is simply $d\mathbf{p}(\mathbf{x})/dt=\mathbf{g}n^{\sigma}(\mathbf{x})$, where $\mathbf{g}$ is the gravitational constant. The new momentum is then

$$n^{\sigma}(\mathbf{x})\mathbf{u}'(\mathbf{x})=n^{\sigma}(\mathbf{x})[\mathbf{u}(\mathbf{x})+\tau_{\sigma}\mathbf{g}] . \tag{17}$$

As an initial test of this force term we try to simulate Poiseuille flow where a constant body force drives a fluid

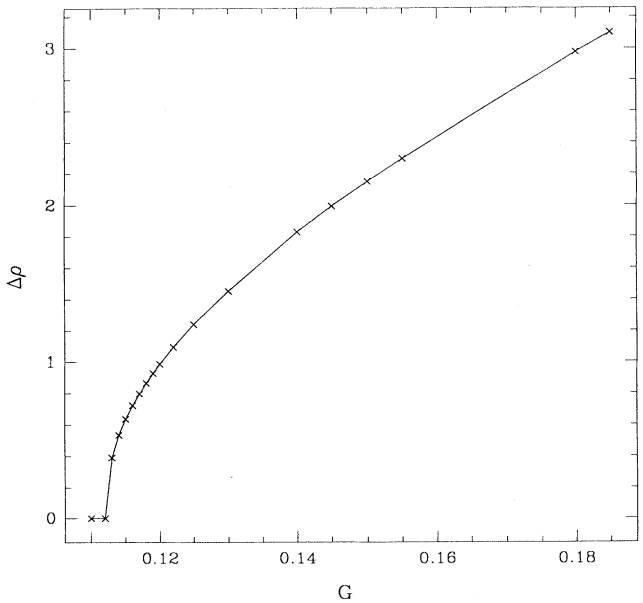

FIG. 1. Phase diagram showing the maximum difference of a single fluid's density $\Delta\rho$ (here $m=1$) as the interaction potential's strength G is varied. The ×'s correspond to data from numerical simulations. The solid line is included to guide the eye. The phase transition takes place near the predicted value of $G_c=\frac{1}{9}$.

between two parallel plates. The simulation should produce a parabolic [23] velocity profile with the maximum velocity in the center of the plates. Figure 2 shows a velocity profile generated in our simulation. The solid line is a fit to a parabola. To obtain the so-called no-slip boundary condition (zero velocity at the wall) it is common practice to use the "bounce-back" [24] method where all particles hitting the wall are reflected back. This method is only accurate to first order in the velocity fields. Note that our solution, which is accurate up to second order, was obtained by constructing a distribution of particles at the pore-solid interface with zero net velocity at the wall. Here the distribution of particles going out from the wall are set equal to their complementary incoming velocity distributions while the complementary distributions in the plane of the wall are set equal to their average value producing a zero velocity equilibrium distribution. This new distribution is then evolved according to Eq. (3). Recently, improvements over the bounce-back method have also been made by Noble *et al.* [25], which produce solutions of second-order accuracy.

VI. FLUID SEPARATION: SURFACE TENSION FORCE

The fluid-fluid interaction can be modeled by using $\psi=n^{\sigma}(\mathbf{x})$ with $G_{\sigma\sigma}=0$ and $G_{\sigma\bar{\sigma}}\neq 0$ for $\sigma\neq\bar{\sigma}$ so that

$$\frac{dp^{\sigma}}{dt}(\mathbf{x})=-n^{\sigma}(\mathbf{x})\sum_{\sigma'}^{S} G_{\sigma\sigma'}\sum_{a=0}^{b} n^{\sigma'}(\mathbf{x}+\mathbf{e}_a)\mathbf{e}_a \ . \tag{18}$$

By varying G we can control the surface tension force between the fluids. At large enough G two mixed fluids separate and a well defined interface forms between the fluids of order two or more lattice spacings depending on the strength of G.

The pressure change across a fluid-fluid interface δP is well described by Laplace's [21] law

$$\delta p=\gamma\kappa \ , \tag{19}$$

where γ is the surface tension and κ is the local curvature. For a spherical drop $\kappa=2/r$, where r is the radius of the sphere. SC demonstrated, in two dimensions, that the pressure difference across the interface of fluids forming circular disks of varying radii was consistent with Laplace's law (here $\kappa=1/r$). To test our 3D code a series of spherical drops were generated and the difference in pressure inside and outside the drop was determined. Figure 3 shows the pressure difference vs the curvature of several different radius drops generated in our simulation, which is in good agreement with Laplace's law.

VII. FLUID-SOLID INTERACTION

To describe the interaction between a fluid and a wall we introduce the interaction force

$$\mathbf{f}^{\sigma}(\mathbf{x})=-n^{\sigma}(\mathbf{x})\sum_{a} G_a^{\sigma} s(\mathbf{x}+\mathbf{e}_a)\mathbf{e}_a \ , \tag{20}$$

where $s=0$ or 1 for a pore or a solid, respectively. By adjusting the interaction strength G_a^{σ} (positive for nonwetting fluid and negative for wetting fluid) for each fluid we control which fluid preferentially wets a surface.

A contact angle θ is defined as the angle made at the point the fluid-fluid and the fluid-solid interface meet. Typically, a fluid is regarded as wetting for small contact angle and nonwetting if the contact angle is large. We find that reasonably well defined contact angles may be obtained by adjusting the interaction strength G_a^{σ} for each fluid such that one of the fluids wets a surface. Figure 4 shows different static contact angles, obtained in our simulations for different values of G^{σ}. While any

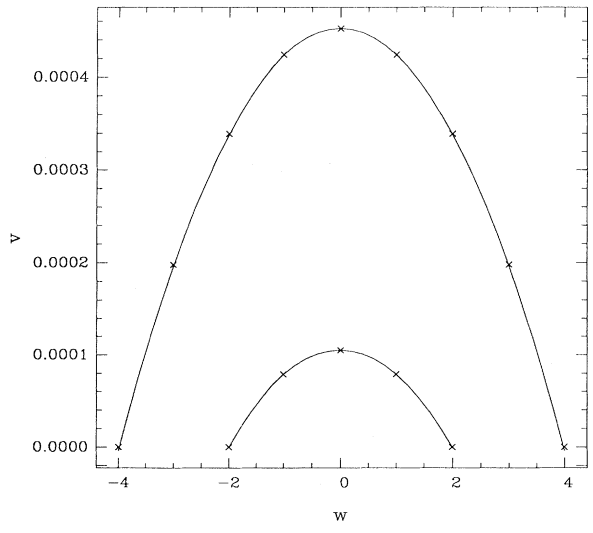

FIG. 2. Velocity profile obtained using the constant force term of Eq. (16). The velocity is v, in units of (lattice spacing)/(unit time step), and w is the distance from the center of the channel in units of lattice spacing. The crosses are from the simulation and the line is a fit to a parabola.

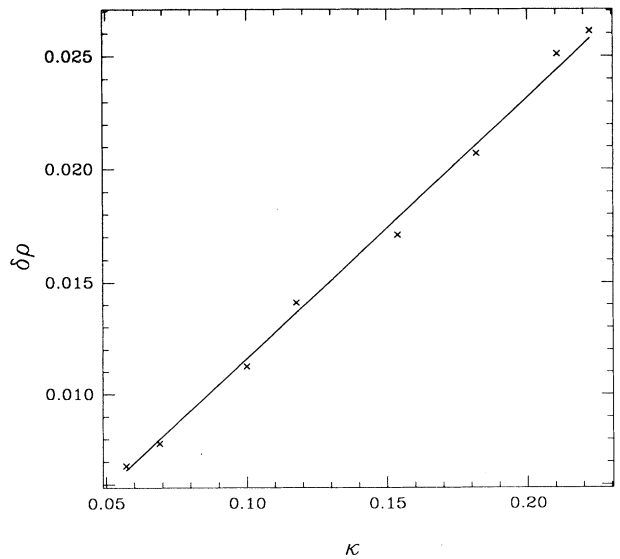

FIG. 3. Change in density (here $m=1$) across the surface of a spherical droplet ($\delta\rho$) vs its curvature (κ). The slope of the line is proportional to the surface tension.

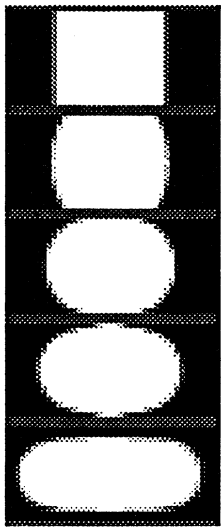

FIG. 4. Change of static contact angle as surface tension forces are varied. The dark area represents one fluid and the light area a second fluid. The two fluids are sandwiched between two plates. In the top panel the surface energies are the same for both fluids. In each successive lower panel the surface energies are adjusted so that the two-fluid interface relaxes to a different static contact angle. In the bottom panel the dark fluid completely wets the surface.

static contact angle may be obtained, there is no guarantee that fluid dynamics near the contact line is correctly simulated. Careful consideration must be made of several issues such as the correctness of the interaction potential, the equilibrium distribution, and the resolution near the fluid-solid boundary. Further research is needed to determine how well our approach can model contact line motion and what modifications may be needed.

VIII. FLOW IN POROUS MEDIA

With all the necessary forces determined, we are able to model multicomponent fluid flow in porous media. The porous medium used in this study was derived from a high resolution microtomography image of a Fontainebleau sandstone [26]. Due to limits in computer memory the microstructures used in the simulations were 64^3 subsections of the original 224×288^2 microstructure where the lattice spacing was of order 7.5 μm. The porosity was approximately 15.2%.

Two cases were studied. In the first case we consider the morphology of an invading nonwetting (wetting) fluid that displaces a wetting (nonwetting) fluid in the porous medium. In this simulation quasiperiodic boundary conditions were maintained in the direction of the applied force such that any fluid exiting the porous medium reenters at the inlet and is converted to (or relabeled as) the injected wetting (nonwetting) fluid. As a result, the total momentum and volume of both fluids is kept constant at the boundaries. Periodic boundary conditions at the inlet and outlet of the porous media were obtained by either introducing a gap (a region of no solid) at the inlet and outlet of several lattice spacings or by constructing a mirror image of the porous medium across the plane between the inlet and outlet.

Figures 5(a)–5(c) shows the pore space, the pattern formed by the invading nonwetting fluid, and the pattern formed by the invading wetting fluid, respectively. In Figs. 5(b) and 5(c) approximately 50% of the available pore space has been invaded by the fluid. Note the dramatic difference in the pattern formation. In the case of nonwetting invasion, the invading fluid pushes out the wetting fluid by entering a pore and filling the region somewhat like an expanding balloon filling a cavity. In this process the nonwetting fluid gradually pushes out most of the wetting fluid, except that near the solid surface.

In the case of wetting invasion, the wetting fluid moves along the surface and often traps the nonwetting fluids, which is unable to escape through the smaller pores [see Fig. 5(d)]. Our simulations are consistent with experiments [27] that demonstrate that residual saturation of a wetting fluid (for nonwetting invasion) may be considerably smaller than the residual saturation of a nonwetting fluid (wetting invasion).

Since the computational time needed to reach steady state in these injection simulations is very long (of the order of weeks on typical workstations) we used an alternative approach to determine the relative permeability for the wetting and nonwetting fluids as a function of saturation. The two fluids were initially introduced in a uniform manner throughout the pore space (a similar approach was used by Gunstensen and Rothman [28] and Auzerais *et al.* [26]). The relative permeability for each fluid (wetting or nonwetting) was then determined as a function of its saturation. The advantage of this method is that steady-state flow is reached in a much shorter time interval, allowing for substantially more simulations. The disadvantage is that by initially starting the system as a mixture many regions may be more accessible than if we had tried displacing one fluid by another, thus leading to a different fluid morphology.

In general, we could calculate the relative permeability by taking the ratio of the volumetric flow rate of the partially saturated system to the volumetric flow rate of the fully saturated porous medium for a given fluid and applied force. However, we found that in many cases the response (change in volumetric flow rate with respect to driving force) of the fluid to an applied force was not linear. For example, at intermediate saturations the nonwetting fluid exhibited pinning effects at low driving forces, resulting in little or no flow. To determine the relative permeability in this case, a large enough applied force was used such that the response to the applied force was linear. The relative permeability was then calculated by taking the ratio of the slopes of the volumetric flow rate vs driving force curve for the partially saturated system and the fully saturated one.

Values of relative permeability, obtained from simulation on a 64 cubed system for different saturation of wetting and nonwetting fluids, are shown in Fig. 6. Included are values from relative permeability experiments [27] carried out on the same Fontainebleau sample used to generate the microtomography image that was utilized in

our simulations. Agreement is quite good despite the smallness of our system (relative to that used in the experiments) and difference in initial conditions. Due to local variation of the pore structure, system size is important in the determination of macroscopic parameters such as permeability [26]. Also, assuming that the porous medium is homogeneous at a large enough length scale, calculations of permeability using several smaller systems will produce a distribution of permeability values that becomes narrower as system size is increased. From

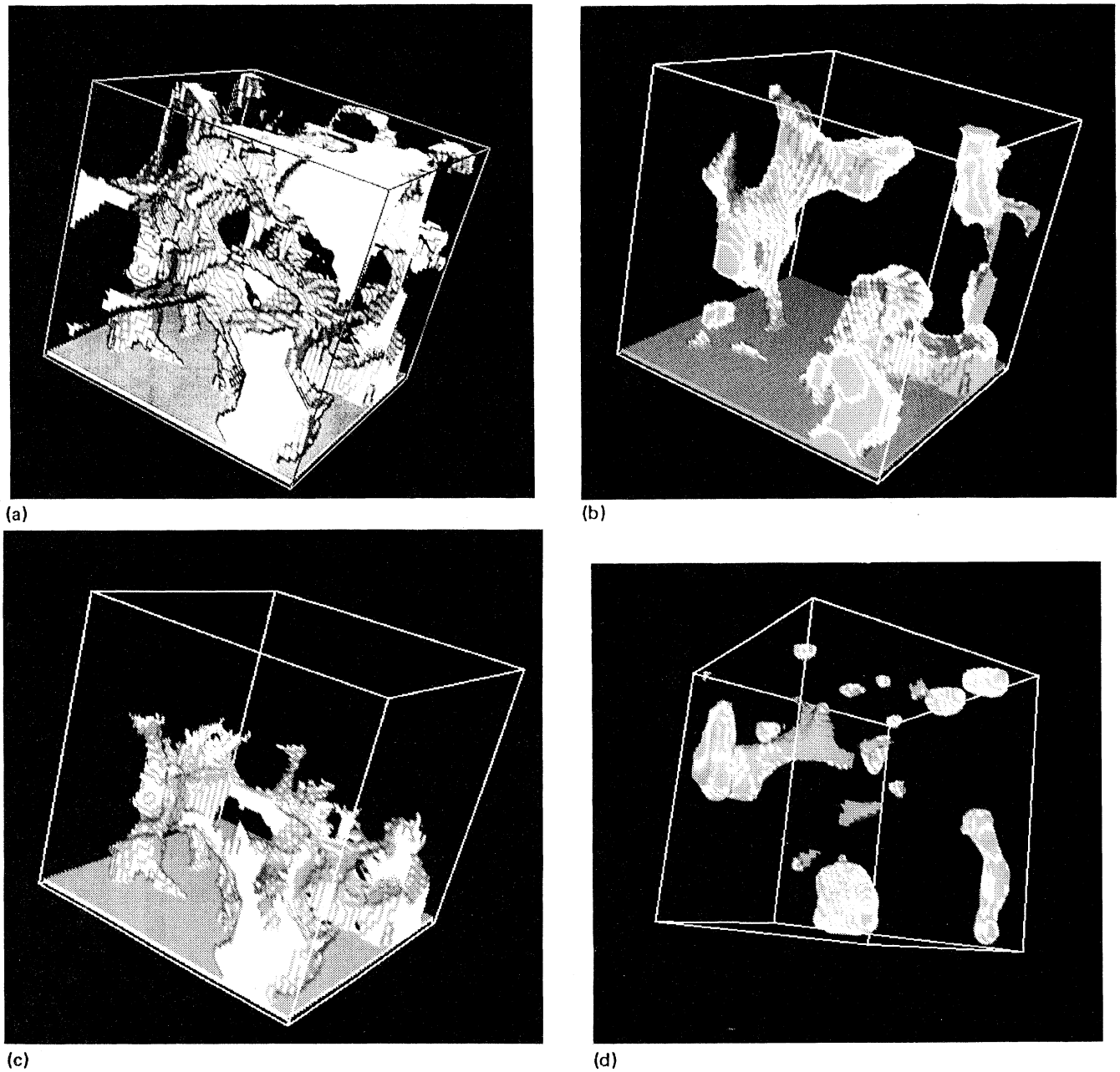

FIG. 5. (a) Pore structure, obtained by x-ray microtomography techniques, used in fluid invasion simulations. The light region represents the pore space. The solid portion was made transparent to reveal the pores. The porosity is 15%. The small plane of pore space at the bottom is where the invading fluid enters. (b) Pattern formed by a nonwettting fluid displacing a wetting fluid in the pore space shown in (a). The nonwetting fluid fills the pores similar to a balloon expanding in a cavity. (c) Pattern formed by a wetting fluid displacing a nonwetting fluid in the pore space shown in (a). The rougher appearance of the pattern formed by the wetting fluid is due to it moving primarily along the solid surface. (d) Remaining blobs of nonwetting fluid as a wetting fluid displaces a nonwetting fluid. Most of the blobs are pinned in the porous media. However, those near the top of the image will exit. When steady state was reached, close to 18% of the remaining fluid was trapped nonwetting fluid.

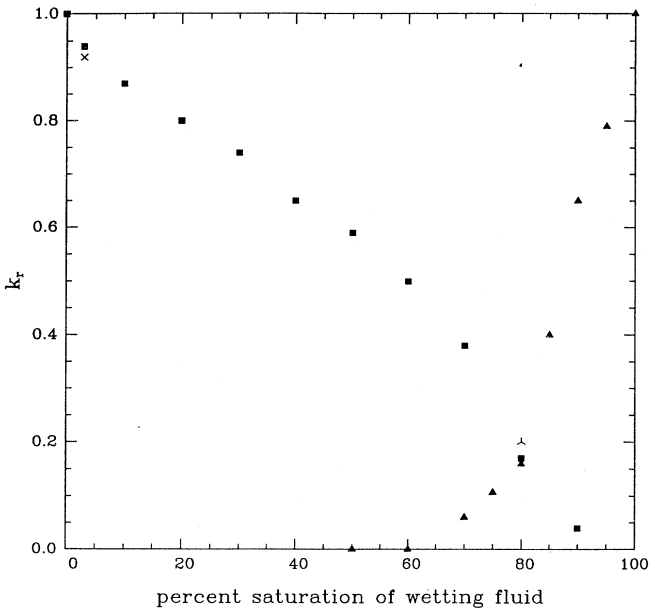

FIG. 6. Relative permeability values k_r for different saturations of wetting fluid in sandstone. The filled squares correspond to the nonwetting fluid relative permeability. The filled triangles correspond to the wetting fluid permeability. The inverted box and triangle correspond to experimental data provided by T. S. Ramakrishnan of Schlumberger-Doll.

additional simulations on five different 64^3 sections of the sandstone image we found, for the case of an 80% saturation of wetting fluid, that the average relative permeability was about 0.27 ± 0.12, where the $\pm$ value corresponds to the spread of values obtained (the experimental value was approximately 0.2). Given the resolution of our image, it is doubtful that accurate estimates of the relative permeability of the wetting fluid can be obtained at low values (below 60%) of saturation of our sample. Since the wetting fluid is most likely to reside along a surface forming a thin layer, our simulations cannot accurately represent the flow of the wetting fluid without further improvement of resolution. Further studies include the dependence of relative permeability calculations on system size and resolution.

While at least qualitatively similar results have been obtained by Gunstensen and Rothman [28], Fcrréol and Rothman, [29] and Chen *et al.* [15,30] using different lattice Boltzmann methods, it is not clear how well their estimates of relative permeability would directly compare with experimental data. A favorable comparison to experimental values of relative permeability for nonwetting invasion using the lattice gas method was recently obtained by Olson and Rothman [26]. Here, for comparison, the value of relative permeability k_r obtained by experiment [27] at 97% saturation of nonwetting fluid was 0.92. For the same saturation using the LG method [26], $k_r = 0.95$, while we obtained $k_r = 0.94$ using the LB method described in this paper. Despite the good agreement with experiment, the nonwetting saturation in this case is so high it is not clear if this saturation regime provides a stringent test of either LG or LB methods. However, our calculations of the wetting fluid's relative permeability show a dramatic drop in relative permeability at moderately high saturations (80%), as seen in experiments (see Fig. 6), indicating that our LB simulation methods capture at least some of the important features of the multicomponent fluid transport.

IX. CONCLUSION

We have applied the formalism of SC to the modeling of multicomponent fluid flow in complex geometries such as porous media. Reasonably good agreement between our simulation values of relative permeability and experimental data was found. An advantage of this formalism is perhaps its simplicity and transparency in interpretation of how to include external interactions. While our results are encouraging, future research includes the testing of this method for flow of nonideal gases, fluids with a viscosity mismatch, three-phase flow, and improved accuracy of calculations near the solid surface.

ACKNOWLEDGMENTS

The authors would like to thank Dr. J. Bullard of the National Institute of Standards and Technology, J. Olson and Dr. D. H. Rothman of the Massachusetts Institute of Technology, and Dr. T. S. Ramakrishnan and Dr. L. M. Schwartz of Schlumberger-Doll for useful discussions. We would also like to thank J. Dunsmuir of Exxon Research and Engineering Company, L. M. Schwartz, and T. S. Ramakrishnan for providing the x-ray microtomography image of the Fontainebleau sandstone.

APPENDIX

The D3Q19 model corresponds to the case where the velocity of particles is limited to the following directions in three dimensions: $(\pm 1,00)$, $(0,\pm 1,0)$, $(0,0,\pm 1)$, $(\pm 1,\pm 1,0)$, $(\pm 1,0,\pm 1)$, $(0,\pm 1,\pm 1)$, and (0,0,0). Here there are a total of 19 components with the last corresponding to rest particles. The 4D FCHC lattice model limits velocities of particles to $(\pm 1,0,0,\pm 1)$, $(0,\pm 1,0,\pm 1)$, $(0,0,\pm 1,\pm 1)$, $(\pm 1,\pm 1,0,0)$, $(\pm 1,0,\pm 1,0)$, $(0,\pm 1,\pm 1,0)$, and (0,0,0,0). Here there is a total of 24 components plus one corresponding to the rest particles. As can be seen, D3Q19 is the same as 4D FCHC without the fourth component.

[1] F. A. L. Dullien, *Porous Media: Fluid Transport and Pore Structure* (Academic, San Diego, 1992).
[2] T. Vicsek, *Fractal Growth Phenomena* (World Scientific, Singapore, 1989); *Dynamics of Fractal Surfaces,* edited by F. Family and T. Vicsek (World Scientific, Singapore, 1991).
[3] U. Frisch, B. Hasslacher, and Y. Pomeau, Phys. Rev. Lett. **56**, 1505 (1986); U. Frisch, D. d'Humières, B. Hasslacher, P. Lallemand, Y. Pomeau, and J.-P. Rivet, Complex Syst. **1**, 649 (1987); S. Wolfram, J. Stat. Phys. **45**, 471 (1986); G. McNamara and G. Zanetti, Phys. Rev. Lett. **61**, 2332 91988); F. Higuera and J. Jimenez, Europhys. Lett. **9**, 663 (1989); F. Higuera and S. Succi, *ibid.* **8**, 517 (1989); S. Succi, R. Benzi, and F. Higuera, Physica D **47**, 219 (1991); J. A. Somers and P. Rem, *ibid.* **47**, 39 (1991); S. Chen, Z. Wang, X. Shan, and G. D. Doolen, J. Stat. Phys. **68**, 379 (1992); D. O. Martinez, W. H. Matthaeus, S. Chen, and D. C. Montgomery, Phys. Fluids A (to be published).
[4] D. H. Rothman and S. Zaleski, Rev. Mod. Phys. **66**, 1417 (1994).
[5] S. Chen, H. Chen, D. Martinez, and W. H. Matthaeus, Phys. Rev. Lett. **67**, 3776 (1991).
[6] K. Molvig, P. Donis, J. Myczkowski, and G. Vichniac, in *Discrete Kinetic Theory, Lattice Gas Dynamics and Foundations of Hydrodynamics,* edited by R. Monaco (World Scientific, Singapore, 1988).
[7] Y. H. Qian, D. d'Humières, and P. Lallemand, Europhys. Lett. **17**, 479 (1992).
[8] Y. H. Qian and S. A. Orzag, Europhys. Lett. **21**, 255 (1993).
[9] H. Chen, S. Chen, and W. H. Matthaeus, Phys. Rev. A **45**, 5339 (1992).
[10] P. L. Bhatnager, E. P. Gross, and M. Krook, Phys. Rev. **94**, 511 (1954).
[11] D. H. Rothman, Geophysics **53**, 509 (1988).
[12] D. Rothman and J. M. Keller, J. Stat. Phys. **52**, 1119 (1988).
[13] A. K. Gunstensen, D. H. Rothman, S. Zaleski, and Zanetti, Phys. Rev. A **43**, 4320 (1991).
[14] A. K. Gunstensen and D. Rothman, Europhys. Lett. **18**, 157 (1992).
[15] Los Alamos Science, Mail Stop M708, Los Alamos National Laboratory, Los Alamos, NM 87545.
[16] U. D'Ortona, D. Salin, M. Cieplak, R. B. Rybka, and J. R. Banavar, Phys. Rev. E **51**, 3718 (1995).
[17] D. Rothman, J. Geophys. Res. **95**, 8663 (1990).
[18] X. Shan and H. Chen, Phys. Rev. E **47**, 1815 (1993).
[19] X. Shan and H. Chen, Phys. Rev. E **49**, 2941 (1994).
[20] For a lattice gas approach to modeling phase transitions see C. Appert and S. Zaleski, Phys. Rev. Lett. **64**, 1 (1990).
[21] G. K. Batchelor, *An Introduction to Fluid Dynamics* (Cambridge University Press, Cambridge, UK, 1967).
[22] X. Shan and G. Doolen, J. Stat. Phys. (to be published).
[23] L. Kadanoff, G. McNamara, and G. Zanetti, Phys. Rev. A **40**, 4527 (1989).
[24] S. Chen, G. D. Doolen, and W.H. Matthaeus, J. Stat. Phys. **64**, 1133 (1991).
[25] D. R. Noble, Shiyi Chen, J. G. Georgiadis, and R. O. Buckius, Phys. Fluids **7**, 203 (1993).
[26] F. M. Auzerais, J. Junsmuir, B. Ferréol, N. S. Martys, J. Olson, T. S. Ramakrishnan, D. H. Rothman, and L. M. Schwartz, Geophys. Res. Lett. (to be published).
[27] Experimental data provided by courtesy of T. S. Ramakrishnan of Schlumberger-Doll. The relative permeability was obtained for the case of water displacing dodecane (wetting displacement) or dodecane displacing water (nonwetting displacement). The viscosity ratio between dodecane and water is about 1.5. In our simulations our viscosity ratio was 1. Since in both experiment and simulation the capillary number was very low, of order 10^{-4} and 10^{-3}, respectively, we do not believe viscous effects (such as viscous fingering) were very important.
[28] A. K. Gunstensen and D. H. Rothman, J. Geophys. Res. **98**, 6431 (1993).
[29] B. Ferréol and D. H. Rothman, Trans. Porous Media (to be published).
[30] S. Chen, K. Diemer, G. D. Doolen, K. Eggert, C. Fu, S. Gutman, and B. J. Travis, Physica D **47**, 72 (1991).

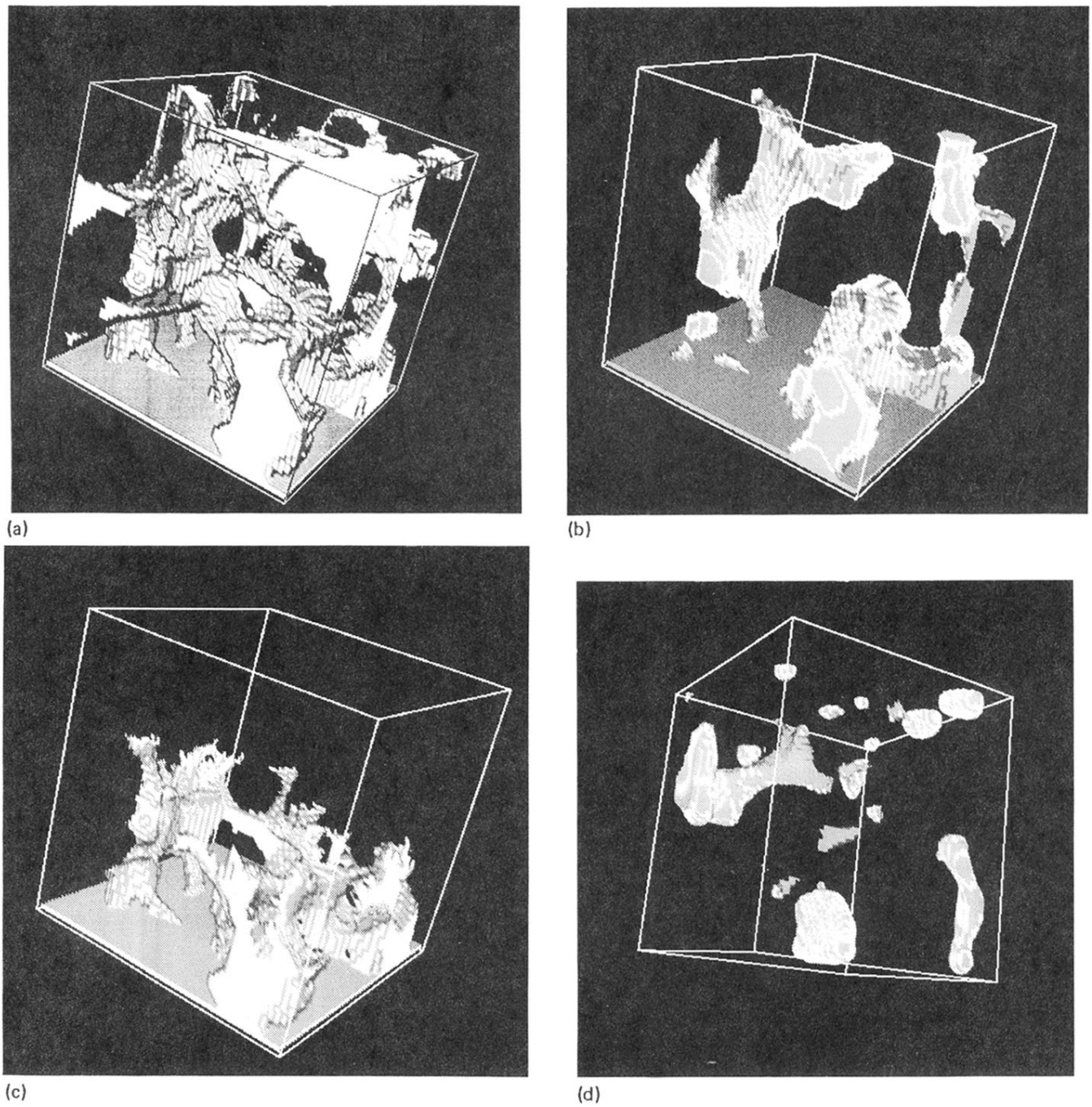

FIG. 5. (a) Pore structure, obtained by x-ray microtomography techniques, used in fluid invasion simulations. The light region represents the pore space. The solid portion was made transparent to reveal the pores. The porosity is 15%. The small plane of pore space at the bottom is where the invading fluid enters. (b) Pattern formed by a nonwettting fluid displacing a wetting fluid in the pore space shown in (a). The nonwetting fluid fills the pores similar to a balloon expanding in a cavity. (c) Pattern formed by a wetting fluid displacing a nonwetting fluid in the pore space shown in (a). The rougher appearance of the pattern formed by the wetting fluid is due to it moving primarily along the solid surface. (d) Remaining blobs of nonwetting fluid as a wetting fluid displaces a nonwetting fluid. Most of the blobs are pinned in the porous media. However, those near the top of the image will exit. When steady state was reached, close to 18% of the remaining fluid was trapped nonwetting fluid.